Monte Carlo study of (gamma ,e gamma) electron momentum densities

Monte Carlo study of $(\gamma, e\gamma)$ electron momentum densities

A J Rollason and M B J Woolf

Department of Physics, Keele University, Keele, Staffordshire ST5 5BG, UK

Abstract. Data are reported for numerical simulations of the triple differential $(\gamma, e\gamma)$ cross-section for inelastic x-ray photon scattering with coincident analysis of recoil electrons from metal foils and thin crystals. Preliminary measurements and calculations have shown that the cross-section is sensitive to the three-dimensional electron momentum density distribution and Fermi surface of the target. These simulations show that a useful signal carried by unscattered recoil electrons is produced from a region near the back of the target and sits on a homogeneous background of multiply scattered electrons. Even for thick samples this background remains sufficiently low due to saturation scattering of the emergent electrons for the umklapp Fermi surfaces in transition metals to be observable with only moderate requirements in statistical accuracy. The present work examines the experimental triple differential cross-section for pseudo-single-crystal targets of Cu and details the resolution and sensitivity of the technique to umklapp regions of the Fermi surface. Figures are presented for the feasibility of measurements at the high-energy beamlines of various synchrotron laboratories.

1. Introduction

Inelastic x-ray scattering studies of electron momentum densities and Fermi surfaces play a central role in condensed matter physics. The cross-sections are closely related to the ground state momentum distribution which is a fundamental property of many-electron systems. Despite great effort made over many years to improve the resolution of traditional Compton scattering experiments, their sensitivity to fine details of the Fermi surface has not significantly changed. A recent development in inelastic scattering called $(\gamma, e\gamma)$ spectroscopy promises to overcome many of the traditional limitations.

In a Compton scattering experiment, the Doppler broadening of inelastically scattered gamma rays is analysed to provide information about the momentum space electronic structure of materials (Williams 1976). The quantity observed is an integral over a plane through momentum space,

$$J(p_z) = \int\int n(p)\, \mathrm{d}p_x \, \mathrm{d}p_y \tag{1}$$

where

$$n(p) = \left| \int \mathrm{d}^3 r \, \mathrm{e}^{-\mathrm{i}p\cdot r} \phi(r) \right|^2 . \tag{2}$$

In the independent particle model, electrons are confined to the region of momentum space within the extended Fermi surface at $p = k_F + G$, where G is any reciprocal lattice vector. Although inherently limited in its momentum sensitivity, the technique has produced high-quality data for testing state-of-the-art bandstructure calculations, for example identifying

dynamic electron correlation processes in the transition metals (Rollason *et al* 1987, Bauer and Schneider 1983).

Figure 1 shows a measurement (Bauer and Schneider 1983) of the Compton profile anisotropy $J_{110}(p_z) - J_{100}(p_z)$ for Cu compared with the prediction due to a bandstructure calculation carried out in the local density approximation (Bagayoko *et al* 1980). The calculation, which has been convoluted with the experimental resolution of 0.41 au (atomic units, $e = \hbar = m = 1$, $c = 137$) fwhm, clearly overestimates the amplitude of the momentum density fluctuations which can be readily traced to the effect of dynamic correlations. Equation (2) can be written in terms of Bloch states to show explicitly the correlation effect.

$$n(p) = \sum |a_G(k)|^2 n(k)\delta(p - k - G) \tag{3}$$

where

$$a_G(k) = \int u_G(r)\,e^{ik\cdot r}\,d^3r$$
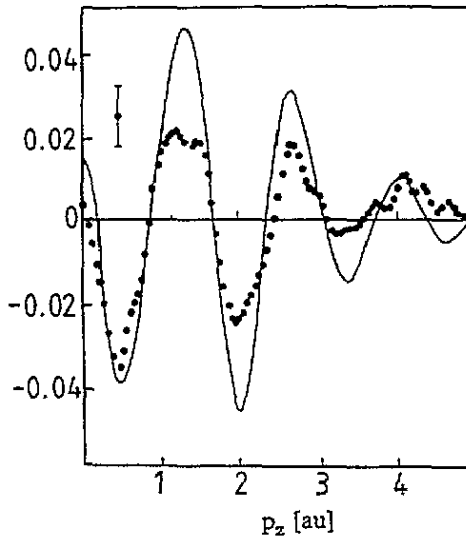
and

$$\psi_k(r) = u_G(r)\,e^{ik\cdot r}.$$

Figure 1. Compton profile anisotropy in copper. The data show the difference between Compton profiles measured in the (110) and (100) directions for single-crystal samples (experiment— circles, Bauer and Schneider 1983, theory—curve, Bagayoko *et al* 1980). The IPA theory neglects dynamic correlations and overestimates the amplitudes of the Fermi surface integrals over planes through the reciprocal lattice points.

In the independent particle approximation (IPA) the spin-independent occupation function is given at ordinary temperatures by

$$n(k) = 2 \qquad k < k_F$$
$$0 \qquad k > k_F$$

where k_F is the Fermi momentum.

The effect of dynamic correlations in a homogeneous electron gas is to reduce $n(k)$ below k_F and to promote electrons to higher k-values. A decrease is observed whenever the Compton plane of integration (equation (1)) intersects the Fermi surface. The Compton profile sensitivity is however low. The scale of the reduction is only 10% and the combination of the momentum plane integration and limited p_z resolution result in effects of at most 1% $J(0)$. To overcome these limitations it is desirable to observe the momentum density directly without integrating over a p_{xy} plane in momentum space and hopefully maintaining a good p_z resolution. The dynamically populated regions outside the Fermi surface can then be examined on their own. $(\gamma, e\gamma)$ spectroscopy analyses the recoil electron in coincidence with the scattered gamma ray thus removing the double integration over transverse momentum components shown in equation (1). This allows in principle the direct measurement of the full, three-dimensional electron momentum distribution $n(p)$ of equation (2) (Rollason *et al* 1989a). Furthermore the relative contribution from core electrons which are delocalized in momentum space is greatly reduced compared to that from the valence electrons.

Figure 2 shows the kinematics of the Compton interaction between an initial photon k and an initial electron p. The photon scatters through an angle θ into state k' and transfers momentum $K = k - k'$ to the electron p'. The component of electron momentum transverse to K remains unchanged during the process. The cross-section for inelastic scattering of an unpolarized photon of 4-momentum k from a monochromatic beam of free electrons of 4-momentum p is given by Jauch and Rohrlich (1955) in natural units $(e = m = \hbar = c = 1, \alpha = 1/137)$ as

$$\sigma = \alpha^2 \frac{1}{2\kappa E' \omega'} \int \mathrm{d}\tau_f \, \delta(p' + k' - p - k) X \tag{4}$$

where

$$\kappa = E\omega - p \cdot k \qquad \kappa' = \kappa - \omega\omega'(1 - \cos\theta)$$
$$X(\kappa, \kappa') = \kappa/\kappa' + \kappa'/\kappa + 2(1/\kappa - 1/\kappa') + (1/\kappa - 1/\kappa')^2$$

and the delta function conserves energy and momentum. The integration in equation (4) is to be performed over all unobserved states τ_f of the scattered photon and recoil electron.
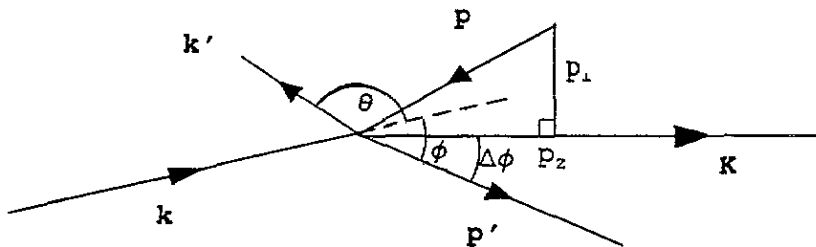

Figure 2. Kinematics of the inelastic photon–electron interaction. θ is the (in general) non-coplanar scattering angle between k and k' and ϕ is the electron recoil angle measured from the incident photon direction k. $\Delta\phi$ is measured from the scattering vector $K = k - k'$.

Equation (4) has been generalized by Eisenberger and Reed (1974) to encompass the distribution of electrons in an atom $n(p)$. Writing the explicit form of the final state integral and conservation laws leads to

$$\sigma = \alpha^2 \int \mathrm{d}^3k' \, \mathrm{d}^3p' \, \mathrm{d}^3p \frac{X(\kappa, \kappa')}{2EE'\omega\omega'} n(p)\delta(p + k - p' - k')\delta(E + \omega - E' - \omega') \tag{5}$$

where the flux factor κ has been replaced by $E\omega$, appropriate for bound electrons of zero mean momentum in the laboratory frame. For initially stationary electrons the recoil direction is along the scattering vector at an angle ϕ_0 to the incident photon beam where $\cot\phi_0 = (1 + \omega)\tan\theta/2$. For moving electrons with transverse momentum $p_\perp$, the recoil direction is given approximately by $\Delta\phi = p_\perp/K$. Compton scattering does not observe the recoil electron direction—only the scattered photon energy and direction are detected—so integrating over p' yields the expression

$$\frac{d^2\sigma}{d\omega'\,d\Omega_{k'}} = \frac{\alpha^2}{2}\frac{\omega'}{\omega}\int d^3p\,\frac{X(\kappa,\kappa')}{EE'}n(p)\delta(E + \omega - E' - \omega'). \tag{6}$$

An approximate result can be obtained from this where the flux factor is taken outside the integral (Ribberfors 1975) giving

$$\frac{d^2\sigma}{d\omega'\,d\Omega_{k'}} \approx \frac{\alpha^2}{2}\frac{\omega'}{\omega}\frac{X_{int}(p_z)}{KE(p_z)}J(p_z) \tag{7}$$

where

$$p_z = \frac{(\omega - \omega') - \omega\omega'(1 - \cos\theta)}{K} \tag{8}$$

K is the momentum transfer $= (\omega^2 + \omega'^2 - 2\omega\omega'\cos\theta)^{1/2}$ and $X_{int}(p_z)$ is derived for an isotropic distribution by integration of the cross-section factor $X(\kappa,\kappa')$. The Compton profile $J(p_z)$ is given by equation (1). Equation (7) is the basis for all Compton scattering experiments with unpolarized photons.

In contrast if the integral over the direction of p is excluded by the process of detecting the recoil electron p', equation (6) leads to

$$\frac{d^3\sigma}{d\omega'\,d\Omega_{k'}\,d\Omega_{p'}} = \frac{\alpha^2}{2}\frac{\omega'}{\omega}\frac{p'}{E}X(\kappa,\kappa')n(p). \tag{9}$$

p_z is again given by equation (8) and $p_{x,y} = p_\perp = K\sin\Delta\phi$. The cross-section allows the momentum density to be measured directly (at least in principle) in a $(\gamma, e\gamma)$ experiment. The momentum resolution element of $(\gamma, e\gamma)$ spectroscopy is three dimensional ($\sigma p_{xy} = 0.05$ au^2, $\sigma p_z = 0.5$ au)—potentially much higher than for Compton scattering ($\sigma p_z = 0.5$ au)—and resolutions comparable to those obtained by measurements of the angular correlation of annihilation radiation (ACAR) should be possible. When the statistical accuracy of the $(\gamma, e\gamma)$ measurement is limited due to a weak photon source or high resolution of the recoil direction, equation (8) may be integrated over the scattered photon energy ω' (which is approximately equivalent to integrating over p_z) to give

$$\frac{d^2\sigma}{d\Omega_{k'}\,d\Omega_{p'}} \approx \frac{\alpha^2}{2}\left[\frac{\omega'_0 K_0}{\omega}\right]^2 X_0 I(p_x, p_y) \tag{10}$$

where

$$I(p_x, p_y) = \int dp_z\, n(p) \tag{11}$$

and the parameters are evaluated at the Compton energy $p_z = 0$. This 2D angular correlation is the $(\gamma, e\gamma)$ counterpart of ACAR measurements.

Equation (9) is strictly valid only for loosely bound electrons where binding energy effects can to a first approximation be neglected. No complete theory yet exists to describe $(\gamma, e\gamma)$ measurements for core electrons but an obvious kinematical effect is the loss of energy by the escape of the photon and electron from a potential well. In principle the energy of the recoil electron can be analysed together with the scattered photon to quantify

the energy loss. This suggests the possibility of obtaining shell-specific momentum densities for the core states or the spectral density function $\rho(p, E)$ and the bandstructure $E(p)$ of the valence electrons which would represent a very powerful technique. Thus in stark contrast to the rather isolated field of Compton scattering $(\gamma, e\gamma)$ data can be directly related to many other fields of experimental condensed matter research including angle-resolved photoemission spectroscopy, ACAR and electron momentum spectroscopy (Williams 1976).

Experiments were originally performed using 300 keV γ-ray sources (Rollason *et al* 1989a,b) but now take advantage of the much higher intensities available at high-energy synchrotrons (albeit at reduced energies, 100 keV–200 keV). The in-plane linear polarization of the synchrotron beam leads to a slight reduction of the cross-section factor X near $\theta = 90°$ but is otherwise insignificant for inelastic scattering. The $(\gamma, e\gamma)$ target is mounted within an evacuated scattering chamber and is observed with an HPGe photon detector and a silicon photodiode electron detector coplanar with the photon scattering plane. Both detectors may be scanned in this plane but most measurements to date have been made with a fixed photon angle of $\theta \approx 140°$ and the electron detector angle ϕ is scanned. (Recently a 2D array of 32 1 cm photodiodes has been used to avoid time-consuming scanning.) The signals from each detector are timed and asserted to be coincident if they occur within a window of a few 100 ns. The photon energy is analysed and stored together with the electron detector position.
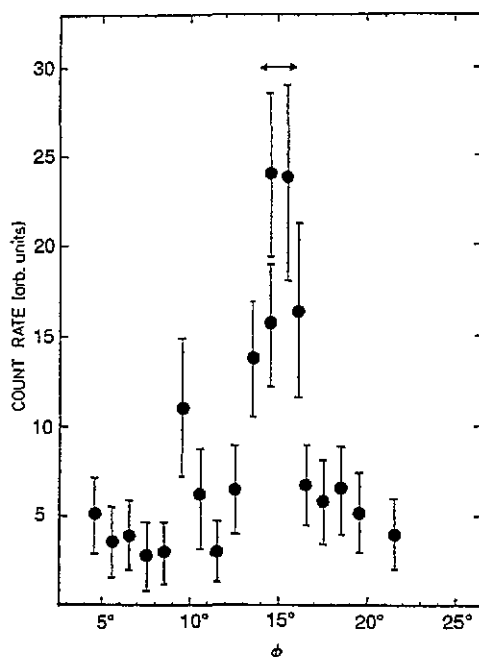

Figure 3. $(\gamma, e\gamma)$ $I(p_x, 0)$ angular correlation curves for aluminium. Data measured at HASYLAB on a 20 μm foil reveal the central correlation peak due to the nearly free Fermi surface sphere whose width (1.86 au) is indicated by the arrows. (Rollason *et al* 1989c.)

Measurements on thin foils of aluminium, copper and carbon, made using the high x-ray energies available at HASYLAB, have demonstrated the validity of the $(\gamma, e\gamma)$ technique and the valence electron momentum densities and Fermi surfaces have been unambiguously identified (Rollason *et al* 1989c, Bell *et al* 1990, Tschentscher *et al* 1993a, b). Figure 3 shows angular correlation data obtained for a 20 μm polycrystalline foil of aluminium. The limits of the central Fermi sphere in this nearly-free-electron metal are quite clear and indicated by the arrows.

Of necessity the Al measurements were made on foils of thickness much greater than the

recoil electron mean free path. The data in figure 3 are for the worst case examined. Other sample thicknesses were studied and all showed a clear agreement over the width of the central Fermi peak. However even the thinnest available Al target (0.12 μm) was optically thick and it was decided to examine an optically thin sample. Graphite was chosen as this can be easily produced as very thin unsupported foils. Figure 4 shows results obtained at HASYLAB (Tschentscher *et al* 1993b) for a 250 Å (0.3 λ) foil. The measured data represent angular correlations both in and perpendicular to the photon scattering plane and the two theoretical profiles are for pyrolytic graphite and randomly orientated diamond structures. There is general agreement with the calculations but the present resolution and statistical accuracy are insufficient to distinguish the curves. The anisotropy shown by the theoretical curves is of the order of 10%—much bigger than ever seen in Compton measurements— and should eventually be readily detectable. In the absence of the required improvements in statistics it can be stated that graphite (a semi-metal) has only a weakly defined Fermi surface and it is more instructive for the development of the technique to study real metals.
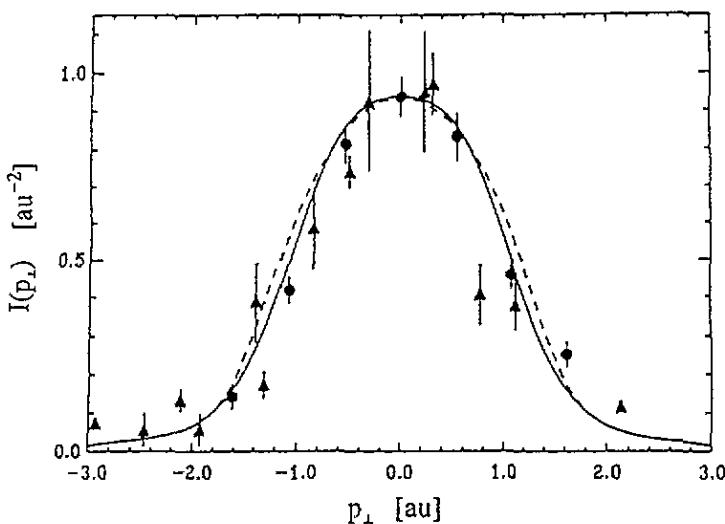

Figure 4. $(\gamma, e\gamma)$ angular correlation curves for 250 Å graphite foils. Experimental data— $I(p_x, 0)$ (circles) and $I(0, p_y)$ (triangles). Theory—pyrolytic graphite (solid curve) and polycrystalline diamond (broken curve). (Tschentscher *et al* 1993b.)

2. Numerical simulations

The simulations are Monte Carlo programmes which model the escape of the Compton recoil electrons from the targets. They are written in the Fortran-77 language and run conveniently on a 66 MHz 486 PC. The code has been developed from original photon scattering simulations (Felsteiner and Pattison 1975) which have been used and updated over many years to correct Compton profile data. Early calculations (Rollason *et al* 1989b) have correctly reproduced the trends in $(\gamma, e\gamma)$ data but are greatly extended here for deeper scattering and accurate geometrical effects.

The controlling parameter in $(\gamma, e\gamma)$ angular correlation measurements is the electron mean free path for scattering at an angle comparable with the desired resolution. Inelastic scattering occurs with a characteristic deviation given by $\Delta E / 2E$ which is of the order of

0.1° for scattering 50 keV electrons from Cu (0.03° from Al) and is therefore in general much more strongly forward directed than elastic scattering. Figure 5 shows the differential incoherent (atomic) elastic cross-sections at 50 keV for Cu and Al. The curves are calculated according to the Mott–Rutherford cross-section (Salvat and Parellada 1984) with electron screening modelled by analytical single-zeta Slater-type orbitals (STOs) matched to Roothan Hartree–Fock wave functions (Clementi and Roetti 1974). The fwhm of these curves corresponds at 50 keV to momentum transfers of around 2 au so that even single scattering events will obscure all details of the Fermi surface and the cumulative result of multiple elastic scatterings is virtually independent of the Fermi surface structure. The elastic cross-section therefore limits the range over which electrons can be ejected from the sample and still give a useful signal. The range is characterized by a mean free path shown as a function of energy in figure 6. The scale is of the order of 100 Å to 1000 Å and is the reason for the very small intensities obtained in $\gamma, e\gamma)$ experiments.
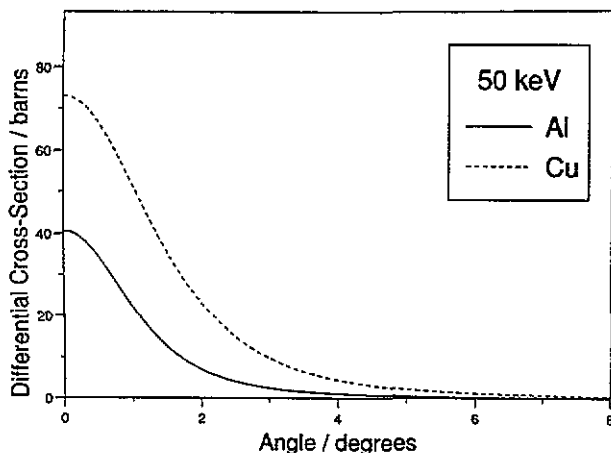

Figure 5. Elastic incoherent scattering differential cross-sections for Cu and Al.

Although the strength of the unscattered signal is limited to a thickness of 1 λ, measurements may still be performed on much thicker (macroscopic) samples. The emerging electrons then undergo many scatterings (plural scattering). When plural scattering occurs the mean deviation is controlled by the rms angle of the elastic scattering cross-section shown in figure 7. At around 100 keV in copper the cumulative effect of 100 scatterings is to produce a truncated Gaussian-like angular distribution of rms width $\sqrt{100} \times 5° = 50°$, corresponding to a 2D fwhm of about 15°. This is very broad compared to features of the Fermi surface (at 100 keV $K \approx 100$ au and $p_F = 1$ au corresponds to an angle of 0.5°, equation (9)) and contributes only a flat background to the signal. Exact details of the distribution are therefore relatively unimportant and a Gaussian shape is appropriate. The simulation follows the path of each individual electron to a depth of 100 multiple scatterings and represents any further plural scattering interactions occurring in very thick samples by such a Gaussian diffuse model.

The real photon interaction rate obeys a very weak exponential attenuation law (photon mean free path $\sim$ 1 cm) and thus all targets will in practice be uniformly sampled throughout their depth by the incident photon beam. The useful information about $n(p)$ however is carried only by the direct (unscattered) recoil electrons which are ejected predominantly from the back surface of the target in a layer about 1 λ_{el} (electrons) thick. For good statistical accuracy in the simulations it is desirable to model the scattering from this region
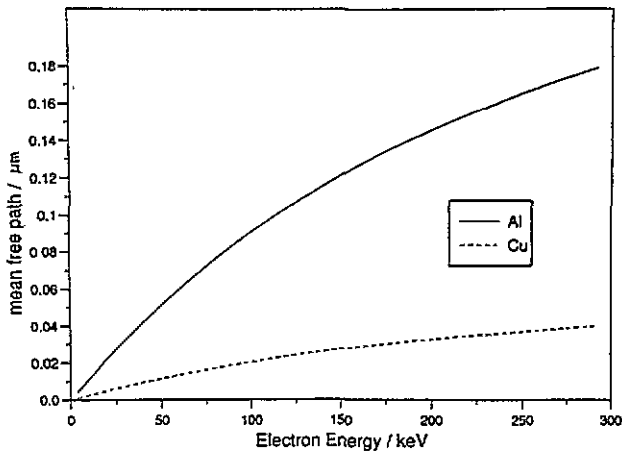
Figure 6. Electron elastic scattering mean free paths in amorphous solids. Useful information in the $(\gamma, e\gamma)$ experiment is conveyed by the unscattered signals from a region less than 1λ thick at the back of the target. Scattered signals produce a uniform background below. This sets a characteristic saturation length of 1λ for the measurement.
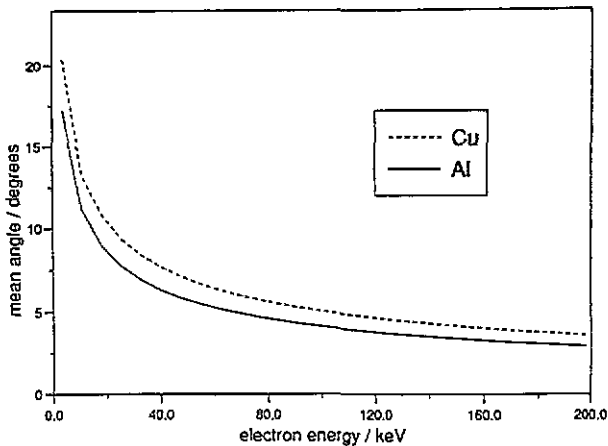

Figure 7. Effective elastic scattering deviation for multiple scattering in Al and Cu. The mean deviation of an electron undergoing N scatterings is equal to $\sqrt{N}\theta_{rms}$.

more carefully than deeper in the target. Thus the photon interaction probability and the corresponding photon weight have been modified to favour frequent interactions at the back of the target as shown in figure 8. The program simulates an effective photon interaction mean free path given by

$$1/\lambda = 1/N\lambda_{el} - 1/\lambda_{ph} \approx 1/N\lambda_{el} \qquad (12)$$

where N is the multiple-scattering limit (modelling diffuse plural scattering beyond this). This ensures that the target is frequently and evenly sampled throughout the statistically sensitive depth where individual multiple-scattering events are followed and less frequently sampled where diffuse plural scattering is modelled analytically. Typical sampling characteristics for a 10 μm Cu target are shown in figure 8. Because the effective photon weight (dotted curve) is decreased as the sampling frequency (dashed curve) increases,

normalization of the total number of incident photons interacting at a particular point (solid curve) is maintained in the statistical limit.

2.1. Momentum density model

The impulse approximation cross-section (equation (5)) describes the interaction of a photon beam with an atomic target in terms of a distribution of electron momenta $n(p)$. The simulation therefore takes the electron momentum density (EMD) of the target as the initial state for the Compton recoil electrons.
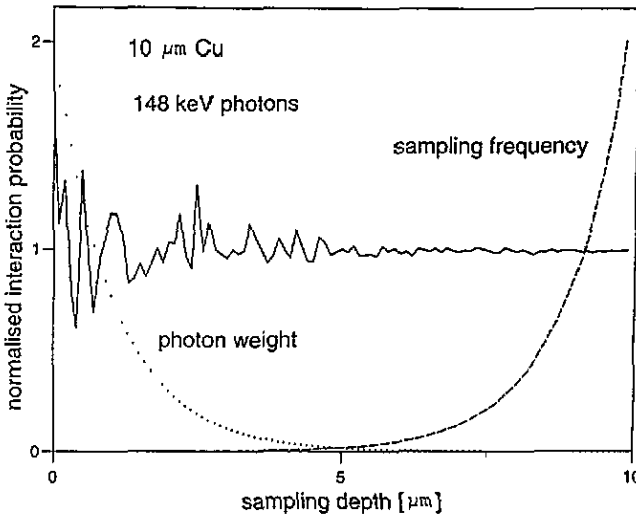

Figure 8. Sampling frequency distribution in a 10 μm copper target. The photon beam energy is 148 keV, giving a photon mean free path of 9.4 mm, whereas the mean free path of the recoil electrons at $\sim$50 keV is only 100 Å (0.01 μm). For a multiple-scattering depth of 100, the frequency of sampling is therefore increased over the last 1 μm of the target to improve statistics and the photon weight is correspondingly reduced. 1.4 million photon interactions were modelled.

For Al a simple free-electron model has been employed for the three conduction electrons with single-zeta STOs (Komarov and Temkin 1976) adopted for the core contribution.

$$n_{1s}(p) = \frac{2^3}{\pi^2} \frac{\zeta^5}{(\zeta^2 + p^2)^2} \qquad \zeta = 12.59 \text{ au}$$

$$n_{2s}(p) = \frac{2^3}{3\pi^2} \frac{\zeta^5(3\zeta^2 - p^2)^2}{(\zeta^2 + p^2)^6} \qquad \zeta = 4.107 \text{ au}$$

$$n_{2p}(p) = \frac{2^7}{3\pi^2} \frac{\zeta^7 p^2}{(\zeta^2 + p^2)^6} \qquad \zeta = 4.482 \text{ au}$$

$$n_{cond}(p) = 2.67 \qquad p < 0.93 \text{ au}$$
$$0 \qquad p > 0.93 \text{ au}.$$

For Cu the anisotropy in the conduction electron momentum density has been modelled by a Seitz model (figure 9) in the same manner as by Pattison *et al* (1982). These authors approximated the $a_G(k)$ in equation (3) by fitted band averages, independent of k, which was shown to be capable of reproducing the gross features of the anisotropy of the Fermi

surface. For the present study such an approximate but realistic momentum density is quite adequate and the model has been fitted at the first 27 reciprocal lattice vectors to a LCGO momentum density (Sundararajan 1993), giving the values $|a_{000}|^2 = 0.426$ au^{-3}, $|a_{111}|^2 = 0.055$ au^{-3}, $|a_{200}|^2 = 0.048$ au^{-3} and $|a_{220}|^2 = 0.024$ au^{-3}. The core electrons are again modelled by STO functions.

$$n_{1s}, n_{2s}, n_{2p} \text{ as above with } \zeta_{1s} = 28.33 \text{ au}, \zeta_{2s} = 10.53 \text{ au}, \zeta_{2p} = 12.55 \text{ au}$$

$$n_{3s}(p) = \frac{2^8}{5\pi^2} \frac{\zeta^9(\zeta^2 - p^2)^2}{(\zeta^2 + p^2)^8} \qquad \zeta = 5.156 \text{ au}$$

$$n_{3p}(p) = \frac{2^8}{45\pi^2} \frac{\zeta^7 p^2(p^2 - 5\zeta^2)^2}{(\zeta^2 + p^2)^8} \qquad \zeta = 4.876 \text{ au}$$

$$n_{cond}(p) = \sum |a_G|^2 n(k)\delta(p - k - G) \qquad k_F = 0.72 \text{ au.}$$

Such a model reproduces the general structure of the EMD as seen in the Compton profile anisotropy but does not yield the fine structure of the Fermi surface due to the (111) necks for example. This omission is unimportant here since the aim is to show that structures of dimensions equivalent to those of the real Fermi surface remain detectable in the $(\gamma, e\gamma)$ measurements.
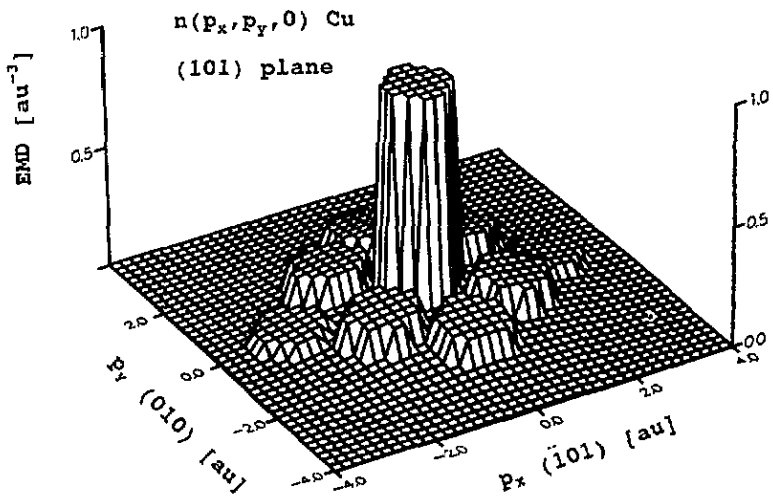

Figure 9. Seitz model electron momentum density of copper. Coefficients for the band-averaged occupation numbers are modelled on the data from Sundararajan (1993).

2.2. Energy losses

No attempt has been made in the present simulations to model the energy losses due to inelastic scattering of the recoiling electrons. The main justification for this is that to date the energy resolution of $(\gamma, e\gamma)$ measurements does not warrant it. Typical energy resolutions are 0.5 keV for the HPGe photon detector and 5 keV for the silicon photodiode electron detector. The major loss mechanism is through plasmon excitations at a rate of ~ 10 eV per mean free path which is longer than the elastic mean free path; a target thickness of at least 500 mean free paths (>5 μm in Al) is required before the energy loss is at present even detectable. Other contributory factors are as follows.
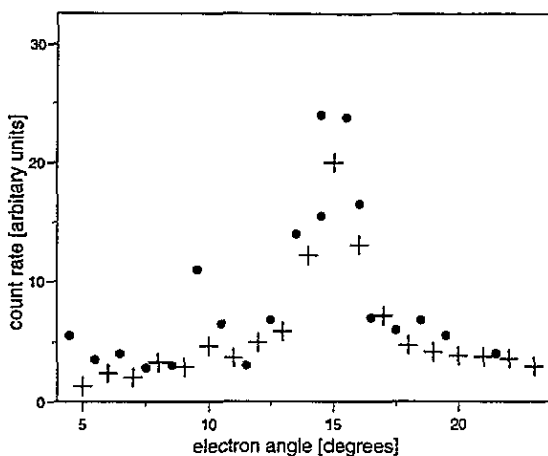
Figure 10. (γ, eγ) angular correlation curves at 144 keV for a 20 μm polycrystalline aluminium foil. Measurement (circles) taken from Rollason *et al* (1989c), simulation (crosses).

Inelastic scattering is more forward directed than elastic scattering, the rms angle varying as $\Delta E/2E$ where ΔE is a characteristic energy of the scatterer and E is the incident electron energy. For Al the effective mean excitation energy is $\Delta E \sim 200$ eV and at 50 keV the mean deviation due to inelastic scattering is only $\sim 0.1°$. Together with the longer mean free path, inelastic interactions therefore produce much less scattering than elastic ones. The inclusion of inelastic scattering would make the multiple-scattering background more diffuse at the expense of a small loss of transmitted signal. The electrons which do lose energy will be even more widely scattered than the higher-energy ones and thus even less observable in the 3D angular correlation. Multiple inelastic scattering therefore tends to remove electrons from the detector.

At least for amorphous solids, experimental multiple-scattering backgrounds should be slightly more homogeneous than the present conservative simulations. The inclusion of energy losses should therefore make the experiment more feasible than the conclusions reached in the present study. Eventually it is hoped that the energy resolution of the photon and electron detectors can both be improved sufficiently to discriminate the energy losses due to inelastic scattering. This is possible because the sum of the final state energies must equal the incident photon energy less the electron binding energy. Plasmon energy losses should appear as a Poisson distribution of peaks spaced at ~ 10 eV leading up to a zero-loss peak. By careful analysis much of the noise contributed by inelastically scattered electrons can then be subtracted from the measurement.

3. Results

3.1. Polycrystalline aluminium

As a system with a very simple Fermi surface (a sphere of radius $p_F = 0.93$ au) Al has been examined several times at different energies by (γ, eγ). A comparison of simulations of polycrystalline Al foils with the experimental data shows good agreement. Rollason *et al* (1989a) describe radioisotope measurements made at 320 keV and figures 10 and 11 give results for measurements at HASYLAB (Rollason *et al* 1989c, Tschentscher *et al* 1993a) for incident photon energies of 144 keV and 100 keV, respectively.
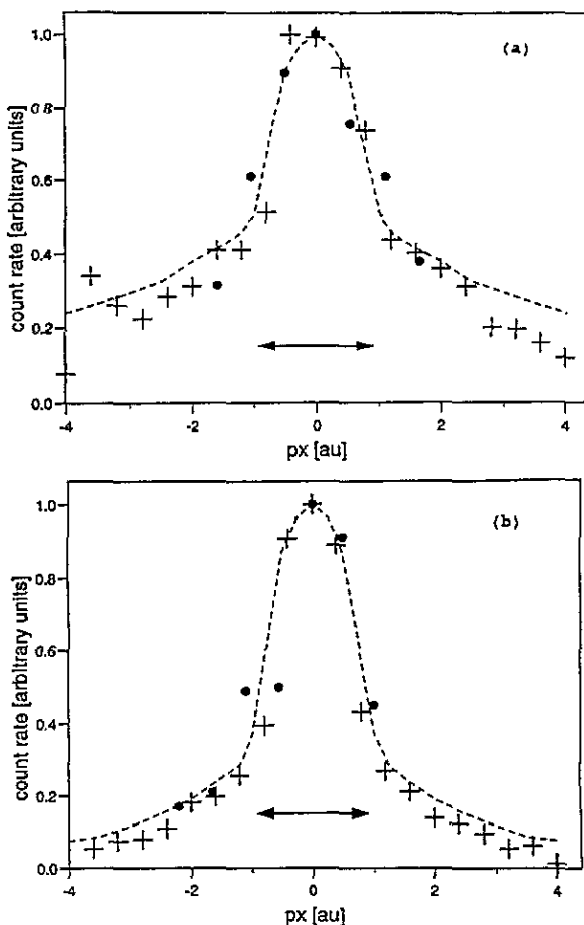
Figure 11. $(\gamma, e\gamma)$ angular correlation curves at 100 keV for (a) 1.85 μm and (b) 895 Å aluminium foils. Experimental data (circles) and calculation (dashed curve) by Tschentscher *et al* (1993a), present simulation (crosses).

The figures show 2D angular correlation curves $I(p_x, 0)$ (equation (11)) where the width of the Fermi sphere is indicated in figure 11 by the arrows. Figure 11 shows the results of the present simulations as well as those from an analytical model of $I(p_x, 0)$ based on the Komarov–Temkin STOs (Tschentscher *et al* 1993a) which includes a simple multiple-scattering correction. Clearly in both figures the experimental data are reproduced by the simulations. As the sample thickness increases the same signal appears sitting above a slowly increasing multiple-scattering background. The calculations are normalized to the experimental data peaks; however, within the limits of error in estimating the incident beam intensities, the present simulations are also able to predict the observed integrated count rates. This will be seen to be a useful feature for planning future experiments (see tables 1 and 2).

It has been the tendency to measure 2D angular correlation curves as in figures 10 and 11 whenever the statistical accuracy of the data is limited. However a few 3D-resolved measurements have been made along just one line through momentum space. Figure 12 shows $n(0, 0, p_z)$ data for Al measured at 151 keV (Rollason *et al* 1989c) on a bending

Table 1. Signal rates predicted for $(\gamma, e\gamma)$ measurements on Cu for 10^{15} incident photons. The experiment parameters are $\omega = 148$ keV, $\theta = 140°$, $\Delta\Omega_{k'} = 0.2$ msrad, $\Delta\Omega_{p'} = 14$ msrad. The pixel resolution for columns 6 and 7 is $\Delta p_x = \Delta p_y = 0.17$ au, $\Delta p_z = 0.9$ au.

t (μm)	Photon singles	Electron singles	Direct coincs	Scattered coincs	$n(0, 0, 0)$ ($\pm 20\%$)	$I(0, 0)$
0.01	16×10^3	14×10^3	10 000	3 000	20	40
0.10	16×10^4	61×10^3	18 000	36 000	35	70
1.00	16×10^5	89×10^3	17 000	61 000	35	80
10.0	16×10^6	13×10^4	20 000	69 000	35	100
100	16×10^7	13×10^4	20 000	69 000	35	200

Table 2. Synchrotron operating fluxes and $(\gamma, e\gamma)$ measurement lifetimes. Column 5 is the measurement time required to obtain the counts in table 1.

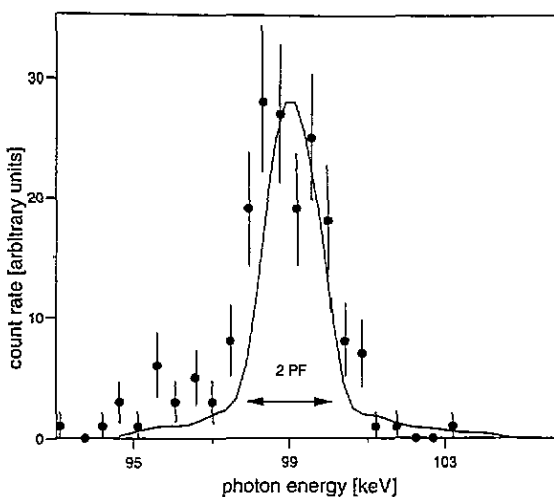| Synchrotron	Station	E (keV)	Flux (photons s^{-1} mm^{-2} keV^{-1})	Measurement time
ESRF	AMPW	150	5×10^{11}	1/2 hour
ESRF	SCWS	150	2×10^{11}	1 hour
HASYLAB	BW2	150	5×10^9	1 day
SRS	16.3	120	1×10^9	1 week

Figure 12. $n(0, 0, p_z)$ data for 0.12 μm aluminium foil. The data include a core contribution and multiple-scattering background arising in a 3 λ thick target but the profile is clearly dominated by the central Fermi sphere (indicated by the arrows).

magnet beamline at HASYLAB. The curve is a Monte Carlo calculation convoluted with the photon energy resolution of 0.7 keV and normalized to the peak of the measurement. The 3D momentum resolution of the measurement is (0.7 au, 0.7 au, 0.7 au). Core contributions become negligible compared to the conduction band in this type of measurement. The Fermi surface sphere is prominent in the experimental data and its diameter although barely measurable is in agreement with the calculation. More recent measurements at wiggler stations show greatly improved statistics; nevertheless, a full 3D measurement along axes

through different parts of momentum space will require the parallel detection capability of a 2D array electron detector.

3.2. Single-crystal copper

The coincident photon energy distribution $n(0, 0, p_z)$ for copper is shown in figure 13. Figure 13(a) compares the simulated photon distribution with data from Bell *et al* (1991) for a polycrystalline foil with an electron detector diameter equivalent to 1.2 au and a p_z resolution of 1 au. Again the statistics are rather poor but there is general agreement on the central width of the correlation peak. This is remarkable since the data represent a 10 λ thick measurement. Figure 13(b) investigates the theoretical dependence on target thickness for a (110) orientated single-crystal target where the results are arbitrarily normalized at the peak. The dashed curve in figure 13(b) is the photon singles intensity, i.e., Compton profile, simulated by the present Seitz model (the dips at 97 and 99 keV are partly due to limiting the model to only 27 Brillouin zones). Although this model is clearly unsuitable for describing the momentum density outside the Fermi surface which is sampled by the Compton profile, it is presented here to illustrate the differences in width and sensitivity to the Fermi surface compared to the momentum density. It can be concluded that the Fermi surface will be observable in such a three-dimensional momentum measurement.

Figure 14 shows the simulated angular correlation for a 1 keV peak band of scattered photon energies for crystalline copper targets of thicknesses (a) 0.01 μm, (b) 0.1 μm, (c) 1 μm and (d) 10 μm. The targets are orientated such that the (101) plane is normal to the photon scattering vector. The primary photon energy is 148 keV, the scattering angle 140 degrees and the collimation is very tight (beam spot 0.2 mm diameter, photon detector acceptance 2 μsrad). The simulated electron detector is a planar 2D array of 51 × 51 0.8 mm pixels situated 30 cm behind the the sample centred on the scattering vector. Each simulation was run on a 66 MHz 486 PC for a duration of ~1 day processing several $\times 10^6$ photons. Multiple elastic scattering was simulated to a depth of 100 interactions and diffuse plural scattering modelled beyond that.

The data for the thinnest target (figure 14(a)) which is only 1 λ thick represent unscattered direct recoil electrons. For this and the 0.1 μm target the umklapp Fermi surfaces are visible and even the thickest target (figure 14(d), 1000 λ) gives a strong central Fermi surface signal. The calculations become statistically worse for the thicker targets where the code spends more time simulating the diffusely scattered background generated far from the surface. In a real experiment the statistics would not deteriorate and a clear trend would emerge of a signal from the Fermi surface sitting above a slowly rising background which becomes saturated at about 10 μm. The inclusion of energy losses in the simulation would cause the background intensity to decrease and saturate for thinner targets for the reasons given earlier.

The resolution of the data in figure 14 (displayed on a 0.17 au × 0.17 au grid) is high with fwhm $\Delta p_x = 0.05$ au, $\Delta p_y = 0.04$ au, bandwidth $\Delta p_z = 0.9$ au and requires a very high flux of photons focused onto a small beam spot. The data are normalized to a simulated incident photon flux of 10^{20} photons which can be realized only at the most intense synchrotron beam lines employing focusing optics. However, relaxing the geometrical constraints slightly to produce a 1 mm beam spot and observing this with an 8 mm photon detector ($\Delta\Omega_{k'} = 0.2$ msrad) gives the resolution function shown in figure 15(a) with fwhm $\Delta p_x = 0.4$ au, $\Delta p_y = 0.3$ au and allows useful measurements to be obtained for an incident photon flux of only 10^{15} photons in 1 day's beam time. Figures 15(b) and 15(c) show the momentum density $n(p_x, p_y, 0)$ obtained with this resolution for
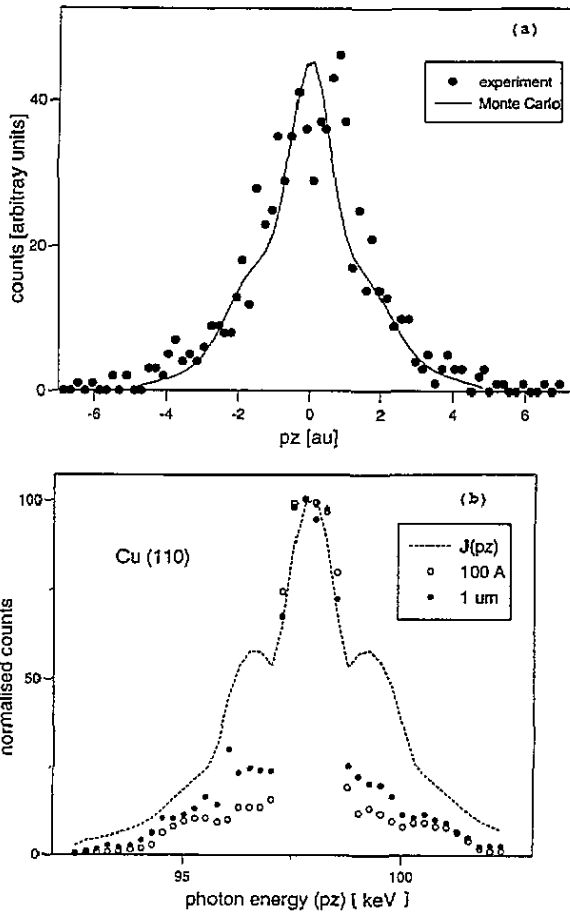
Figure 13. $n(0, 0, p_z)$ for copper. (a) Comparison with experiment (Bell *et al* 1991).
(b) Variation with target thickness.

the two thinnest targets. There is a significant increase in the signal intensity compared to
figure 14 and the resolution is still adequate to see most of the Fermi structure. However
the multiple-scattering background in the thicker target (figure 15(c)) saturates at a higher
level with this new collimation and so either the target thickness or the collimation should
be restricted in actual measurements.

Tables 1 and 2 list some statistics for $(\gamma, e\gamma)$ measurements on Cu at 148 keV, 140° with
a 2D momentum resolution of (0.4, 0.3) au and a pixel resolution of (0.2, 0.2, 0.9) au. The
data are normalized to 10^{15} photons. The maximum pixel count rates are of the order of 100
per 10^{15} incident photons so measurements at the ESRF will produce statistical accuracies
of about 5% at the peak in 1 day. The flux at 120 keV quoted for the SRS would be too low
to obtain accurate 3D momentum density measurements and even data from HASYLAB
have only been obtained with a slightly lower resolution than described here. However the
fluxes increase rapidly as the energy is descreased which makes these measurements feasible
at the lower-energy synchrotons. Mirrors and focusing optics facilitate matters considerably
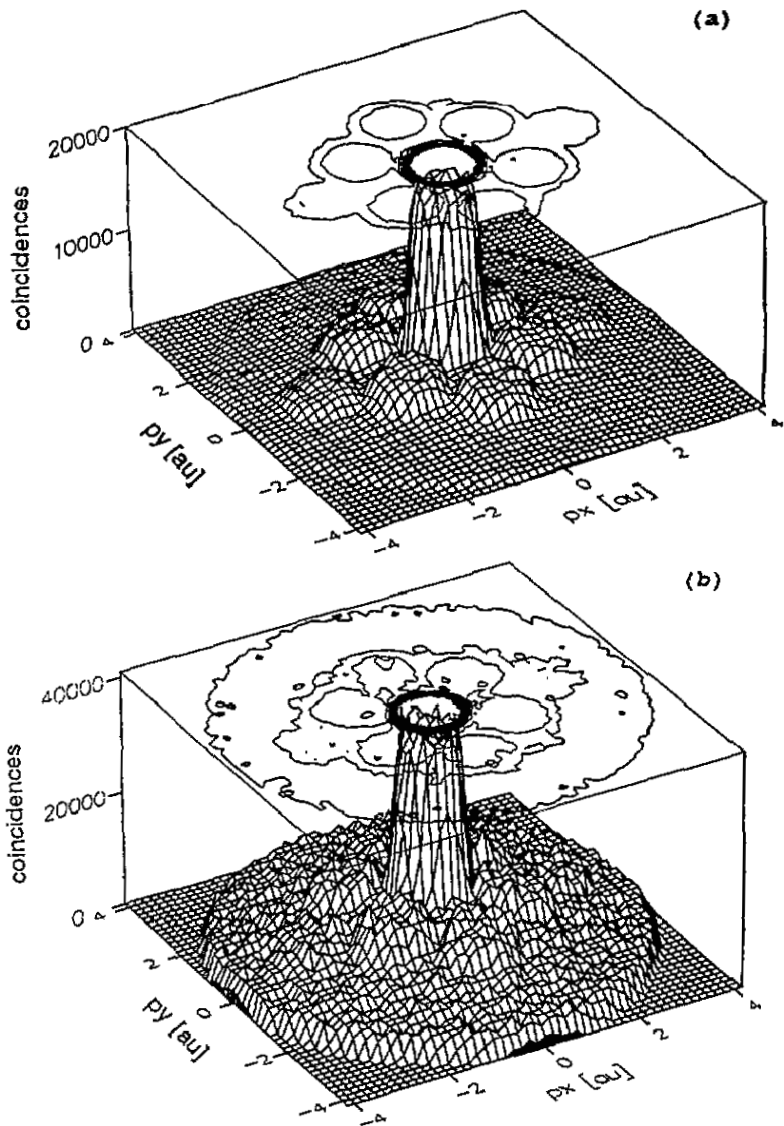but higher-resolution measurements will obviously demand very intense photon beams.

Figure 14. $(\gamma, e\gamma)$ EMD for crystalline copper foils of (a) 100 Å, (b) 0.1 μm, (c) 1 μm and (d) 10 μm. The pixel size corresponds to 0.17 au for p_x and p_y and the photon energy band width of 1 keV corresponds to a 0.9 au slice through the origin.

4. Conclusions

Only a simple model of the initial state momentum density and subsequent electron recoil has been investigated here in line with a similar approach which has been adopted for many years for the accurate analysis of Compton profile data. The overriding aim has been to demonstrate the possibility of obtaining useful signals from the momentum density in optically thick targets. The effects of crystal structure on the electron scattering (Kikuchi bands, diffraction peaks) require further careful study as does the cross-section for photon scattering from spin polarized electrons where work by Lipps and Tolhoek (1954) suggests
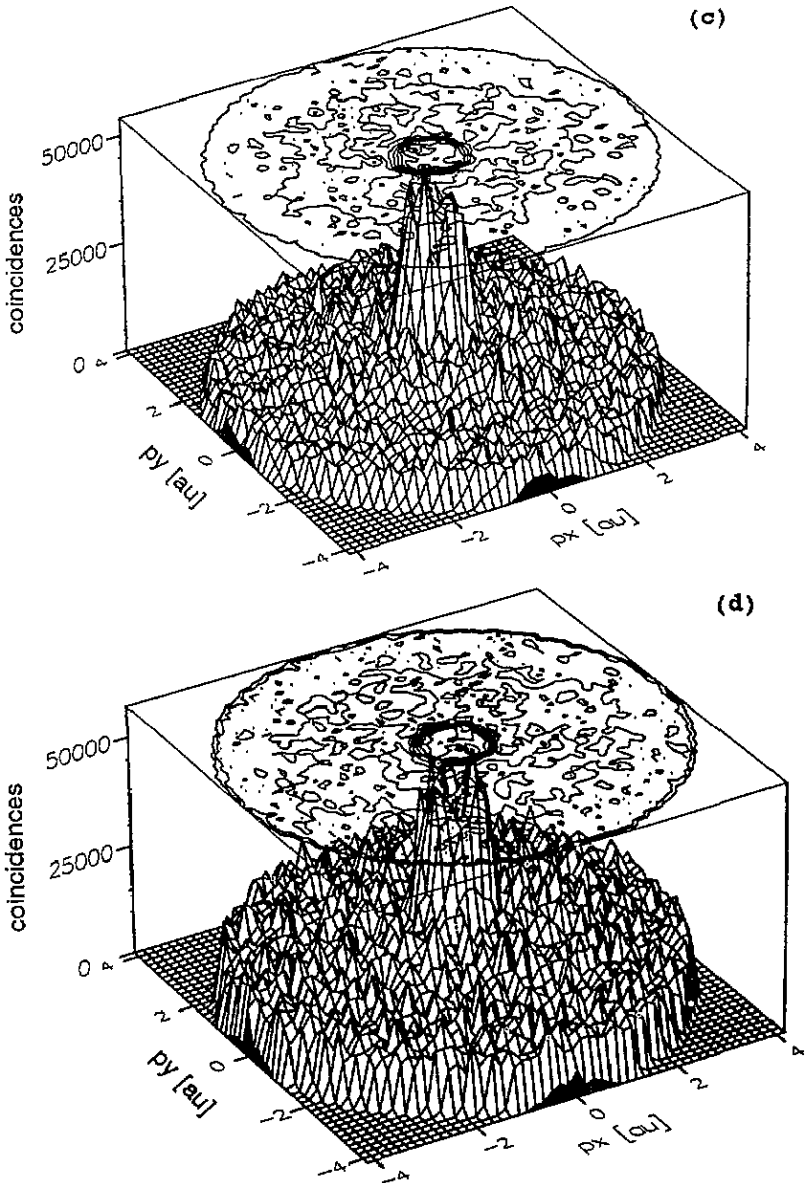
Figure 14. (Continued)

that the spin polarization should be present in the recoil state. Efficient detection of the recoil electron spin in a (γ, eγ) experiment would then allow measurement of the spin momentum density. The energy losses of the emerging electrons due to ionizing interactions and plasmon excitation will also require investigation if energy analysis of the angular correlation in terms of the spectral momentum density is to be performed.

In the absence of these new developments some final conclusions may be drawn about the feasibility of (γ, eγ) measurements. The 3D Fermi surface signal is evident in targets of even 1000 λ thickness and the smooth multiple-scattering background is seen to be approaching saturation. Although simulations on thicker samples are computationally
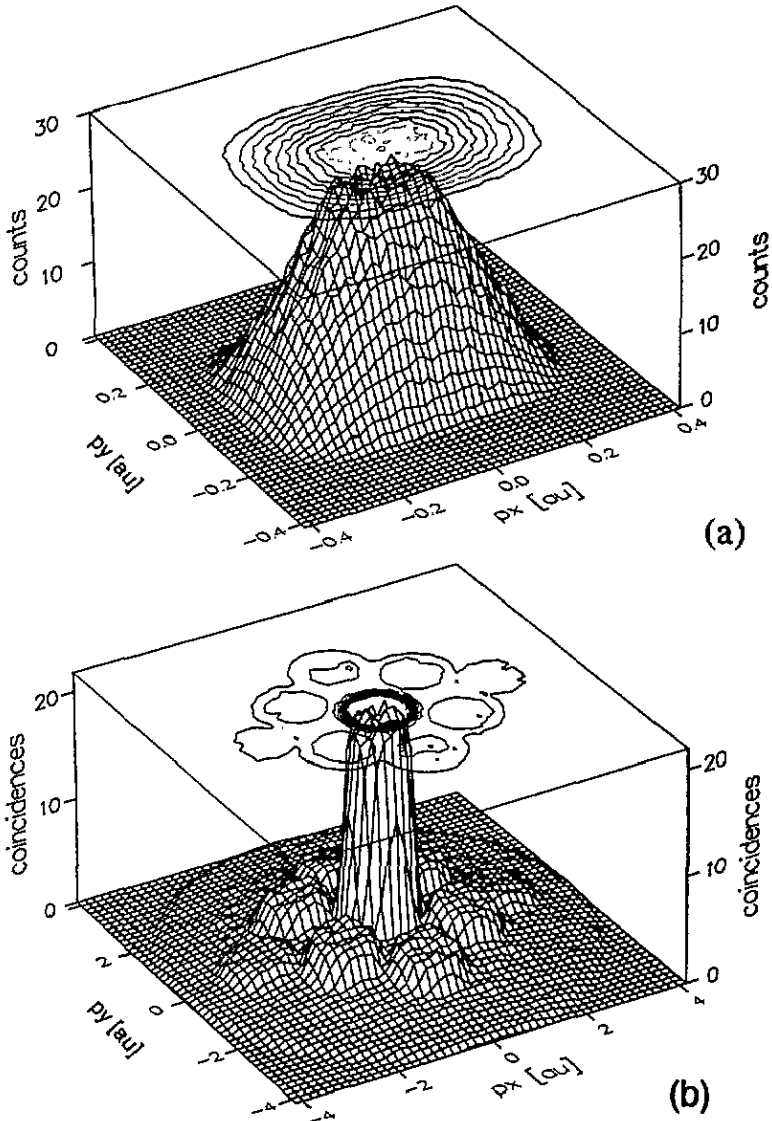
Figure 15. (a) Resolution function $I^0(p_x, p_y)$ and momentum density $n(p_x, p_y, 0)$ for 100 Å (b) and 0.1 μm (c) Cu(101) targets in low-resolution/high-intensity geometry. ($I^0(p_x, p_y)$ is obtained for direct recoil electrons only.)

prohibitive it seems reasonable to assume that there is in principle no limit to the sample thickness which will yield a clearly discernible Fermi surface signal. Providing the background due to accidental coincidences can be kept sufficiently low, this means that single-crystal targets need not be impossibly thin. Readily available single crystals of >0.1 mm thickness should be usable.

Adequate statistical accuracy (a few %) can be achieved for an incident photon flux of 10^{16}–10^{17} photons which is available at third-generation synchrotrons in 1 day (or less if focusing is used). The major requirement is that the recoil electrons should be detected using a 2D array position sensitive detector. All data measured so far have been obtained
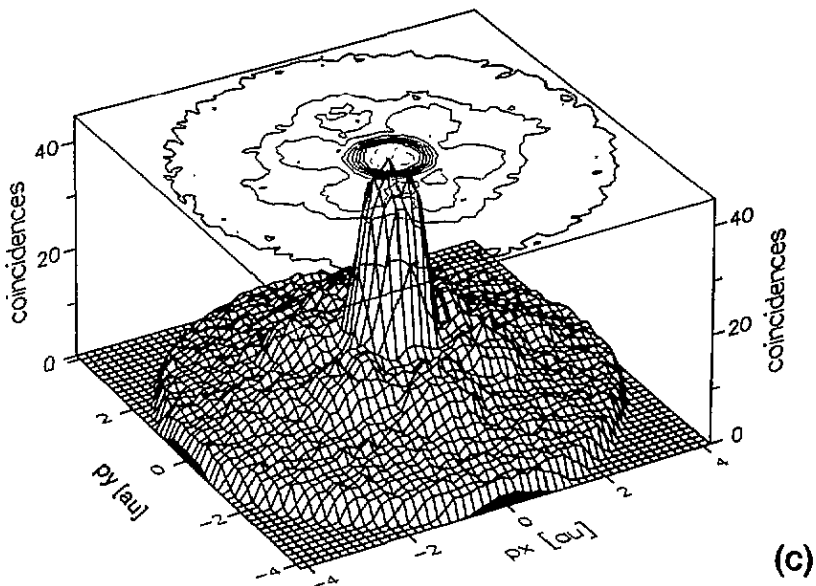
Figure 15. (Continued)

using either a single-pixel PIPS photodiode scanned to determine the angular correlation or at most an array of 32 photodiodes (four rows of eight). Demanding an ultimate position resolution of about 100×100 pixels will require some kind of multiplexed detector such as a double-sided PIPS microstrip wafer or multiwire chamber with 100 orthogonal detector elements on each side.

It is intrinsically impossible to improve the experiment much by continually increasing the incident photon intensity since the single-particle count rates are already high. With increasing incident intensity the detectors experience worse dead time problems and the accidental coincidence count rate becomes too high for the time resolution of the coincidence circuits. Efficient use of low-intensity sources is to be preferred. The count rates can be improved somewhat by increasing the beam spot diameter and placing the two detectors further from the target but the increased count rate may be only a factor of 10 greater before the apparatus dimensions become impractical. (This is a solution adopted for high-resolution ACAR measurements where the detectors are about 10 m from the sample.) A greater enhancement may be achieved by replacing the photon detector with a second position sensitive $N \times N$ array and essentially carrying out N^2 simultaneous correlation experiments. This makes the most efficient use of the x-ray source and should enable measurements with weaker x-ray sources, in particular the SRS.

Acknowledgment

References

Bagayoko D, Laurent D G, Singhal S P and Calloway J 1980 *Phys. Lett.* 76A 187
Bauer G E W and Schneider J R 1983 Z *Phys.* B 54 17

Bell F, Rollason A J, Schneider J R and Drube W 1990 *Phys. Rev.* B **41** 4887

Bell F, Tschentscher Th, Schneider J R and Rollason A J 1991 *J. Phys. B: At. Mol. Opt. Phys.* **24** L533

Clementi E and Roetti C 1974 *At. Data Nucl. Data Tables* **14** 177

Eisenberger P and Reed W A 1974 *Phys. Rev.* B **9** 3237

Felsteiner J and Pattison P 1975 *Nucl. Instrum. Methods* **124** 449

Jauch J M and Rohrlich F 1955 *The Theory of Photons and Electrons* (New York: Springer)

Komarov F F and Temkin M M 1976 *J. Phys. B: At. Mol. Phys.* **9** L255

Lipps F W and Tolhoek H A 1954 *Physica* **20** 395

Pattison P, Hansen N K and Schneider J R 1982 *Z. Phys.* B **46** 285

Ribberfors R 1975 *Phys. Rev.* B **12** 2067

Rollason A J, Bell F and Schneider J R 1989a *Nucl. Instrum. Methods* A **281** 147

Rollason A J, Bell F and Schneider J R 1989b *Hahn–Meitner Institute Report* HMI-B 469

Rollason A J, Bell F, Schneider J R and Drube W 1989c *Solid State Commun.* **72** 297

Rollason A J, Schneider J R, Laundy D, Holt R S and Cooper M J 1987 *J. Phys. F: Met. Phys.* **17** 1105

Salvat F and Parellada J 1984 *J. Phys. D: Appl. Phys.* **17** 1545

Sundararajan V 1993 private communication

Tschentscher Th, Schneider J R and Bell F 1993a *Phys. Rev.* B **48** 16965

Tschentscher Th, Schneider J R, Bell F, Rollason A J and Woolf M B J 1993b *Nucl. Instrum. Methods* B **79** 237

Williams B G (ed) 1976 *Compton Scattering* (New York: McGraw-Hill)